

Swift and *XMM-Newton* Observations of the Extraordinary GRB 060729: An afterglow with a more than 100 days X-ray light curve

Dirk Grupe¹,

grupe@astro.psu.edu

Caryl Gronwall¹, Xiang-Yu Wang^{1,2}, Peter Roming¹, Jay Cummings³, Bing Zhang⁴, Peter Mészáros^{1,5}, Maria Diaz Trigo⁶, Paul T. O'Brien⁷, Kim Page⁷, Andy Beardmore⁷, Olivier Godet⁷, Daniel vanden Berk¹, Peter Brown¹, Scott Koch¹, David Morris¹, Michael Stroth¹, David N. Burrows¹, John A. Nousek¹, Margaret McMath Chester¹, Stefan Immler^{8,9}, Vanessa Mangano¹⁰, Patrizia Romano¹⁰, Guido Chincarini¹⁰, Takanori Sakamoto³, Neil Gehrels³

ABSTRACT

We report the results of the *Swift* and *XMM-Newton* observations of the *Swift*-discovered Gamma-Ray Burst GRB 060729. The afterglow of this burst was exceptionally bright in X-rays as well as at UV/Optical wavelengths showing an unusually long slow decay phase ($\alpha=0.14\pm 0.02$) suggesting a larger energy injection phase at early times than in other bursts. The X-ray light curve displays a break at about 50 ks after the burst. The X-ray decay slope after the break is $\alpha=1.29\pm 0.03$. Up to 100 days after the burst we do not detect a jet break, suggesting that the jet opening angle is larger than 23° . In the first 2 minutes after the burst (rest frame) the X-ray spectrum of the burst changed dramatically from a hard X-ray spectrum to a very soft one. We find that the X-ray spectra at this early phase can all be fitted by an absorbed single power law model or alternatively by a blackbody plus power law model. The power law fits show that the X-ray spectrum becomes steeper while the absorption column density decreases. In the blackbody model we find that the temperature changes from $kT = 0.6$ keV at 85 s after the burst to 0.1 keV at 160 s after the burst in the rest frame. In *Swift*'s UV/Optical telescope the afterglow was clearly detected up to 9 days after the burst in all 6 filters and even longer in some of the UV filters with the latest detection in the UVW1 31 days after the burst, which is one of the latest detections of an afterglow by the UVOT. Clearly, a break between a shallow decay slope of about 0.3 and a steeper decay slope of 1.3 is detected in all 6 filters. These breaks appear to occur all within the errors at about the same time, at about 50 ks after the burst. The spectral energy distributions show that there is no spectral development between X-rays and the UV/optical part of the spectrum between 800 s and 500 ks after the burst. During the whole observing period (except for the early time data) the observed optical to X-ray spectral slope is $\beta_{\text{ox}}=0.8$. From this value we derive an intrinsic reddening of $E_{\text{B}-\text{V}}=0.34$ and an intrinsic absorption column density of $N_{\text{H}} = 1.7 \times 10^{21} \text{ cm}^{-2}$ which is in good agreement with the value measured from the X-ray data. In addition to the *Swift* observations we also present and discuss the results from a 61 ks Target-of-Opportunity observation by *XMM-Newton* starting about 12 hours after the burst. These observations show a typical afterglow X-ray spectrum with $\beta_{\text{X}}=1.1$ and absorption column density of $1 \times 10^{21} \text{ cm}^{-2}$.

Subject headings: GRBs: individual(GBR060729)

1. Introduction

Gamma-Ray Bursts (GRBs) are the most powerful explosions in the present-day Universe. With the launch of the *Swift* Gamma-Ray Burst Explorer Mission (Gehrels et al. 2004) in November 2004 a new era in GRB science has started. *Swift* is able to observe the afterglow of a burst with its narrow-field instruments, the X-ray Telescope (XRT, Burrows et al. 2005a) and the UV/Optical telescope (UVOT; Roming et al. 2005), typically within 2 minutes after the detection by the Burst Alert Telescope (BAT, Barthelmy et al. 2005). Several phenomena were discovered by *Swift*, like the occurrence of giant flares during the first 1000 s after the burst (e.g. Burrows et al. 2005b; Falcone et al. 2006) or the canonical light curves of GRB afterglows (Nousek et al. 2006; Zhang et al. 2006).

GRB 060729 was discovered by *Swift* on 2006 July 29 (Grupe et al. 2006) as one of the brightest bursts ever detected in X-rays by *Swift*. Besides GRB 050525A (Blustin et al. 2005), GRB 060218 (Campana et al. 2006), and GRB 060614 (Mangano et al. in preparation), GRB 060729 is the burst with the best UVOT follow up even up to 9 days after the burst in all 6 UVOT filters and even longer in some of the UV filters. In the XRT the afterglow has been detected by more than 100 days after the burst. This is the longest

follow-up observation with a detection of an afterglow ever performed by *Swift*. Similar coverage, but shorter, has only been performed for GRBs 050416A, 060319, and 060614. Even though the burst was bright in the BAT, it was not detected by Konus-Wind (Frederiks, priv. comm.).

Due to the small sun angle in RA (2.2 h) the afterglow was not observed by many ground based optical telescopes. However, with a declination of Dec= -62° the afterglow is circumpolar for most southern observatories, and was observed by the ESO VLT using FORS2 and by Gemini South using GMOS (Thoene et al. 2006). A redshift of $z=0.54$ was determined from the optical spectra by Thoene et al. (2006). GRB 060729 was also observed by ROTSE IIIa, located at the Siding Spring Observatory, Australia, by Quimby et al. (2006), who reported an initial upper limit of 16.6 mag 64 s after the BAT trigger. They were able to detect the afterglow with ROTSE IIIa up to 175 ks after the burst when it was still at 19.4 mag (Quimby & Rykoff 2006), decaying with a slope $\alpha=0.23$. This decay slope is significantly flatter than what has been reported by Cobb & Bailyn (2006) who measured a decay slope in the I band of $\alpha_I=1.5$ based on CTIO 1.3m SMARTS observations.

The paper is organized as follows: In §2 we describe the observations and the data reduction. In §3 we present the data analysis. The discussion of our results is given in §4. Throughout the paper decay and energy spectral indices α and β are defined by $F_\nu(t, \nu) \propto (t - t_0)^{-\alpha} \nu^{-\beta}$, with t_0 the trigger time of the burst. Luminosities are calculated assuming a Λ CDM cosmology with $\Omega_M=0.27$, $\Omega_\Lambda=0.73$ and a Hubble constant of $H_0=71$ km s $^{-1}$ Mpc $^{-1}$ using the luminosity distances D_L given by Hogg (1999) resulting in $D_L=3120$ Mpc. All errors are 1σ unless stated otherwise.

2. Observations and data reduction

The *Swift* BAT triggered on GRB 060729 at 19:12:29 UT on 2006 July 29 (Grupe et al. 2006; Grupe 2006). *Swift's* X-ray Telescope began observing the afterglow 124 s after the trigger. The UVOT started the observations 135 s after the BAT trigger.

The *Swift* XRT observed GRB 060729 in the

¹Department of Astronomy and Astrophysics, Pennsylvania State University, 525 Davey Lab, University Park, PA 16802

²Department of Astronomy, Nanjing University, Nanjing 210093, China

³Astrophysics Science Division, Astroparticle Physics Laboratory, Code 661, NASA Goddard Space Flight Center, Greenbelt, MD 20771

⁴Department of Physics, University of Nevada, Las Vegas, NV 89154

⁵Department of Physics, Pennsylvania State University, University Park, PA 16802

⁶XMM-Newton Science Operations Centre, ESA, Villafraanca del Castillo, P.O. Box 50727, 28080 Madrid, Spain

⁷Department of Physics & Astronomy, University of Leicester, Leicester, LE1 7RH, UK

⁸Astrophysics Science Division, X-Ray Astrophysical Laboratory, Code 662, NASA Goddard Space Flight Center, Greenbelt, MD 20771

⁹Universities Space Research Association, 10211 Wincopin Circle, Columbia, MD 21044

¹⁰INAF-Osservatorio Astronomico di Brera, via E. Bianchi 46, I-23807 Merate, Italy

Windowed Timing (WT) and Photon Counting (PC) observing modes (Hill et al. 2004). The XRT data were reduced by the *xrtpipeline* task version 0.10.4. The WT mode data at the beginning of the XRT observation had to be treated with special care. During the first 20s after the start (130–150s after the BAT trigger) of the WT XRT observation the satellite was still settling causing the target to move on the XRT CCD towards the dead columns at DETX=319–321. In order to correct for the photon losses due to these dead columns we measured the offset of the source at each second and calculated a correction factor according to the losses of the WT mode Point Spread Function (PSF). After 150s after the trigger all WT mode data were corrected by the same factor. Source and Background photons were selected by *XSELECT* version 2.4 in boxes with a length of 40 pixel. For count rates $> 150 \text{ counts s}^{-1}$, however, in the WT mode the data had to be corrected for pileup. In order to correct for pileup for the spectral analysis and the determination of the hardness ratio¹ we excluded the central regions of the PSF at the source position depending on the count rate as described in Romano et al. (2006). For the PC mode data the source photons were selected in a circular region with a radius of $r=59''$ and the background photons in a circular region close by with a radius $r=176''$ in the first segments. For the later data the radii were reduced to $47''$ and $24''$ for the source, and $137''$ and $96''$ for the background. For the spectral data only events with grades 0–2 and 0–12 were selected with *XSELECT* for the WT and PC mode data, respectively. Note that the source photons for the spectral analysis of the PC mode data of the initial segment 000 observation were selected in a ring with an inner radius of $16''.5$ and an outer radius of $71''.0$ in order to avoid the effects of pile-up (e.g. Pagani et al. 2006; Vaughan et al. 2006). The spectral data were re-binned by using *grppha* version 3.0.0 having 20 photons per bin. The spectra were analyzed with *XSPEC* version 12.3.0 (Arnaud 1996). The auxiliary response files were created by *xrtmkarf* and corrected using the exposure maps, and the standard re-

sponse matrices *swxwt0to1_20010101v008.rmf* and *swxpc0to12_20010101v008.rmf* were used for the WT and PC mode data, respectively. All spectral fits were performed in the observed 0.3–10.0 keV energy band.

Background-subtracted X-ray flux light curves in the 0.3–10.0 keV energy range of the *Swift* observations were constructed using the ESO Munich Image Data Analysis Software *MIDAS* (version 04Sep) and by an IDL program that corrects for PSF losses, in particular when the source is located on one of the dead columns on the XRT CCD detector (Abbey et al. 2006). The light curve was binned as follows: the WT mode data with 1000 photons per bin, and the pc mode data with 200 counts per bin in the first days after the burst and 20 or 10 at the end of the observations. The count rates were converted into unabsorbed flux units using energy conversion factors (ECF) which were determined by calculating the count rates and the unabsorbed fluxes in the 0.3–10.0 keV energy band using *XSPEC* as described in Nousek et al. (2006). The XRT data at the beginning of the observation show dramatic spectral changes and require specific ECFs for each time bin. The later data, however, do agree with a typical afterglow spectrum and the count rates were converted by one $\text{ECF}=5 \times 10^{-11} \text{ ergs s}^{-1} \text{ cm}^{-2} (\text{counts s}^{-1})^{-1}$.

The *Swift* UVOT observations of GRB060729 began with the automated “GRB” sequence, which provided finding chart images in White (100 s) and V (400 s), then began cycling through all 6 UV and optical filters starting 739 s after the trigger. GRB060729 remained detectable in all 6 filters for more than 9 days after the trigger, then for 12 days after the trigger in UVW2 ($\lambda_c = 1930\text{\AA}$) and for 31 days after the trigger in UVW1 ($\lambda_c = 2510\text{\AA}$). During the first days after the burst each observation in each single orbit was analyzed. For the later data the images were coadded with *wvotimsum* in order to improve the signal to noise ratio. The data were analyzed with the UVOT software tool *wvotsource*. Due to a bright star (9.4 mag in B, $107''.5$ away from GRB060729) extra caution had to be taken for the source extraction and the background subtraction. Due to the halo of the bright star (Figure 1) we chose a selection radius of $4''$ for the source and $8''$ for the background in all filters. The background region

¹The hardness ratio is defined by $HR = (\text{hard} - \text{soft})/(\text{hard} + \text{soft})$ where *soft* is the counts in the 0.3–1.0 keV band and *hard* is the counts in the 1.0–10.0 keV band, respectively.

circle was placed at a position nearby which was on the rim of the halo. In order to correct for losses due to this small source extraction radius, we did an aperture correction with $V=0.03$ mag, $B=0.05$ mag, $U=0.05$ mag, $UVW1=0.17$ mag, $UVM2(\lambda_c = 2170\text{\AA})=0.15$ mag, and $UVW2=0.15$ mag. All values plotted and listed in this paper take these corrections into account.

GRB 060729 was also observed by *XMM-Newton* (Jansen et al. 2001) for a total of 61 ks (Schartel 2006; Campana & De Luca 2006). *XMM-Newton* started observing the afterglow of GRB 060729 on 2006 July 30 07:41 (44.9 ks after the trigger) to 2006 July 31 01:04 UT (107.5 ks after the trigger). In the European Photon Imaging Camera (EPIC) pn (Strüder et al. 2001) the total observing time was 59.6 ks using the medium light blocking filter. However, due to high particle background during part of the observation only 42.3 ks were used. The observations in the EPIC MOS (Turner et al. 2001) were for a total observing time of 61.2 ks. The MOS1 was using the medium filter while the MOS2 observations were performed with the thin filter. The total observing time in the Reflection Grating Spectrometers (RGS; den Herder et al. 2001) was 61.5 ks. In the Optical Monitor (OM; Mason et al. 2001) the afterglow was observed for 8.3 ks in U, 5×4 ks in UVW1, 3×4 ks in UVM2, and 2×4 ks with the optical grism. Note, that the OM UVW1 and UVM2 filters are slightly different compared with the UVOT UV filters. The *XMM-Newton* data were reduced with the latest SAS version *xmmsas_20060628_1801-7.0.0*.

3. Data Analysis

3.1. Position of the Afterglow

The position of the afterglow measured from the UVOT UVW1 coadded image is
RA (J2000) = $06^{\text{h}}21^{\text{m}}31^{\text{s}}.86$,
Dec (J2000) = $-62^{\circ}22'12''.5$
with a $1''$ error. This position is consistent with the initial analysis of the White and V filter analysis (Immler 2006). The UVW1 position is $1''.1$ away from the X-ray position RA (J2000) = $06^{\text{h}}21^{\text{m}}31^{\text{s}}.75$, Dec (J2000) = $-62^{\circ}22'13''.3$ (with a $3''.5$ 90% confidence error), which was measured for the XRT PC mode data of segment 001 using the new teldef file *swx20060402v001.teldef* as described in Burrows et al. (2006a). This position

deviates by $3''.2$ from the refined position given in Grupe (2006). The most likely reason for this difference is that for the X-ray position given in Grupe (2006) only the PC mode data of the first orbit were used. This is due to the burst during the first orbit being placed on one of the bad columns on the XRT CCD which makes the determination of a position difficult. Figure 1 displays the UVW1 image of the field of GRB 060729. The circle in the upper right inserted image is the $3''.5$ XRT error radius of the X-ray position given above.

3.2. BAT data

Figure 2 displays the BAT light curves in the 15–25 keV, 25–50 keV, 50–100 keV, and 15–100 keV bands (top to bottom) with $T_0=2006$ July 29 19:12:29 UT (Spacecraft clock 175893150.592). GRB 060729 had a $T_{90}=115$ s (Parsons et al. 2006). After the initial peak which was detected by the BAT and which triggered the observation the burst drops back down to the background level. However, two giant peaks are observed at about 60s after the trigger, of which the first one is harder than the second. There is a third peak which peaks about 120s after the trigger. This is the peak of which we see the end of the decay in the XRT (Figure 3). For the spectral analysis the BAT data were divided into 5 bins as listed in Table 1. The first peak is the initial peak the BAT triggered on GRB 060729. As shown in Table 1, the following two peaks that occur between 70 and 124s after the burst are by a factor of 3 stronger than the initial peak. The two last peaks (124–190s after the burst) are also observed simultaneously in the XRT. These data will be discussed in the XRT section.

Table 1 lists the results of the spectral analysis of the 5 peaks. All spectra were fitted by a single power law model. The initial peak has a hard spectrum with a 15–150 keV energy spectra index $\beta_{15-150\text{keV}}=1.05_{-0.32}^{+0.42}$. The two strong peaks between 70–124s after the burst show an interesting spectral behavior. While the first of these peaks (70–88s after the burst) has a rather hard spectral slope with $\beta_{15-150\text{keV}}=0.59 \pm 0.11$, the second of these peaks (88–124s) became softer with $\beta_{15-150\text{keV}}=0.90 \pm 0.11$. The total fluence in the 15–150 keV band is 2.7×10^{-6} ergs cm^{-2} (Parsons et al. 2006) and 2.7×10^{-5} ergs cm^{-2} in

the rest-frame 1 keV – 10 MeV band adding all BAT spectra together (Table 1) and assuming the same power law spectrum as in the 15-150 keV band without any break. With the redshift $z=0.54$ this converts into an isotropic energy in the rest-frame 1 keV – 10 MeV band of $E_{\text{iso}} = 3.0 \times 10^{52}$ ergs. Because we lack observations of the break energy E_{break} and the γ -ray spectrum at higher energies by Konus-Wind this value is an upper limit of the true isotropic energy.

3.3. X-ray data

3.3.1. Temporal analysis

Figure 3 shows the combined BAT and XRT light curve. The light curve clearly shows that XRT began observing the GRB at the beginning of the fourth peak seen in the BAT. The combined BAT + XRT light curve was constructed as described in (O’Brien et al. 2006). Due to the dramatic spectral change within the three minutes of the WT observation, we applied an ECF for each individual bin. However, for the BAT data we applied only on ECF that reflects the main spectrum.

Figure 4 displays the *Swift* XRT light curve, with WT mode data as triangles and PC mode data as crosses. The vertical dashed lines in the figure mark the start and end times of the *XMM-Newton* observations. The general behavior of the light curve can be described as follows: after the initial steep decay with a decay slope $\alpha_1 = 5.11 \pm 0.22$ the light curve flattens at $T_{\text{break},1} = 530 \pm 25$ s with a decay slope $\alpha_2 = 0.14 \pm 0.02$. At $T_{\text{break},2} = 56.8 \text{ ks} \pm 10 \text{ ks}$ the light curve of the afterglow breaks again and continues decaying with a decay slope $\alpha_3 = 1.29 \pm 0.03$. The definitions of the decay slopes follow the descriptions given in Nousek et al. (2006) and Zhang et al. (2006). We do not detect a jet break even 100 days after the burst.

3.3.2. Spectral Analysis

Dramatic spectral change at the beginning

The WT mode data were divided into 21 bins with 1000 source photons in each bin. In order to examine the spectral behavior in more detail, source and background spectra were created for each bin, except for the first 10 bins ($T - T_0 = 130 - 150$ s). In order to avoid the effects of pileup we had to ex-

clude the central pixels for the spectral analysis as described in Romano et al. (2006). However, this procedure reduced significantly the number of source photons in each single spectrum. In order to increase the signal to noise ratio we combined two bins into one for bins 1+2, 3+4, 5+6, 7+8, and 9+10.

Each of the 16 spectra were fitted by an absorbed single power law, blackbody plus power law, and a power law with exponential cutoff model. The results of these spectral fits are listed in Table 2. Figure 5 shows plots of the WT mode data; from top to bottom the count rate, hardness ratio, the X-ray spectral slope β_X from an absorbed single powerlaw fit with a free fit absorption column density N_H , blackbody temperature kT (in keV) from the blackbody plus power law fit, the blackbody radius² R_{bb} and the break energy E_{break} of a power law with exponential cutoff model. The hardness ratio changes from HR=0.6 at the beginning of the observation to HR=-0.56 at the end, indicating a dramatic evolution in the X-ray spectrum within 2 minutes of observing time which translates into 1.3 minutes in the rest frame.

While the spectra during the first 20 s of the WT mode observation are well-fitted by a single power law model, after about 150s after the burst the data are better fit by a blackbody plus power law spectrum. For the absorbed power law fits, all parameters were left free. We found that while the spectra at the beginning of the observation were rather hard with $\beta_X=1.5$ and $N_H=4 \times 10^{21} \text{ cm}^{-2}$, the spectra became very soft with $\beta_X \sim 3.0$ and $N_H=1 \times 10^{21} \text{ cm}^{-2}$. Note that the absorption column density N_H decreases while the energy spectral index β_X becomes steeper - the opposite than what is expected if the spectral slope and the absorption column density were just linked in the fitting program. However, note that especially during the later bins, the spectra are not well fit by a single power law and do require more complicated models.

For the blackbody plus power law model, the absorption parameter was fixed to the Galactic value ($4.82 \times 10^{20} \text{ cm}^{-2}$ Dickey & Lockman 1990) and the hard energy spectral slope to $\beta_X=1.0$. The

²The blackbody radii were derived for each bin from the relation $L = 4\pi R_{\text{bb}}^2 \sigma T^4$, where σ is the Stefan-Boltzmann constant

blackbody temperature changes dramatically from $kT=0.56$ keV at the beginning of the XRT WT observation to 0.11 keV at the end, accompanied by an increase of the blackbody radius from 2.5×10^{12} cm to 16×10^{12} cm. Fitting the data with an absorbed blackbody plus power law model with the absorption column density at $z=0$ set to the Galactic value and at $z=0.54$ set to 1×10^{21} cm $^{-2}$ (see the discussion about the *XMM-Newton* spectral analysis) results in similar values for the temperature. The only differences are that the temperatures tend to be lower by 40 eV and the normalizations are higher.

The change in the X-ray spectra is also displayed in Figure 6 which shows the spectra of bins # 1, 12, 14, and 21. Bin 12 is the bin before the small flare at 170s after the burst and bin 14 is the peak of that flare.

Later PC mode data

All PC mode data can be fitted by a power law model with a energy spectral slope $\beta_X=1.2$ and an absorption column density of about 1.5×10^{21} cm $^{-2}$. This absorption column density is significantly above the Galactic value . The intrinsic absorption column density at the redshift $z=0.54$ is $1.9 \pm 0.4 \times 10^{21}$ cm $^{-2}$.

The XMM-Newton observations

The combined spectra of the *XMM-Newton* EPIC pn and MOS and *Swift* XRT data are shown in Figure 7. The XRT data were selected between 44900 s and 107500 s after the burst. The details of the spectral fits to these data are summarized in Table 3. At these late times, the X-ray spectra were well fitted by absorbed single power law models. An additional blackbody component is not required. However, as a check the spectra were fitted also by a blackbody plus power law model, but at these late times the power law component dominates the spectra. Therefore, we will only discuss the absorbed power law model fits as listed in Table 3.

The obvious difference between the *Swift* XRT and *XMM-Newton* pn and MOS data is the much higher value of the absorption column density. From the free fit absorption column density at $z=0$ we measured an absorption column density

$N_H=15.7 \times 10^{20}$ cm $^{-2}$ in the *Swift* XRT data. This value is about twice as high as what is measured from the *XMM-Newton* EPIC pn and MOS spectra. The EPIC pn is well-calibrated to energies below 0.2 keV (e.g. Haberl et al. 2003). We also applied the *gain fit* model within *XSPEC*, but it did not remove the discrepancy. This discrepancy maybe due to problems with the *Swift* XRT bias maps during the time period 2006 July 21 and 2006 August 3. This bias map problem causes an offset in the gain and therefore compromises the spectral analysis of *Swift* XRT PC mode data during that time period. However, this gain shift does not affect the early *Swift* XRT WT mode data. Due to the better response of the EPIC pn at lower energies we consider the absorption column densities measured by the EPIC pn the most reliable. With the redshift of the burst at $z=0.54$ we can also use the X-ray spectra to determine the intrinsic absorption column density at the location of the afterglow. The intrinsic column densities of all fits are in the order of 1×10^{21} cm $^{-2}$, except for the *Swift* XRT data which again show an absorption column density about twice as high. As we will show later in section 3.5 the absorption column density of 1×10^{21} cm $^{-2}$ is in good agreement to what can be derived from the spectral energy distribution of the afterglow.

In addition to the EPIC pn and MOS data we also analyzed the 2 RGS spectra. We found that the analysis of the RGS continuum spectra agrees within the errors with the pn and MOS data. We did not find any obvious emission or absorption features in the RGS spectra.

3.4. UV/Optical data analysis

The results of the UVOT data analysis are listed in Table 4. Figure 8 shows the results of the UVOT photometry in comparison with the XRT. UVOT was able to follow the afterglow in all six filters up to 9 days after the burst. In UVW1 the afterglow was followed up even 31 days after the burst which translates into 20 days in the rest-frame. This is one of the longest period *Swift's* UVOT has ever detected an afterglow in the optical/UV. Only GRBs 060218 (Campana et al. 2006) and 060614 (Mangano et al. in preparation) were detected at slightly later times than GRB 060729. The reason why GRB 060729 could not be followed for

a longer time is that the afterglow is located on the rim of a halo of a bright B=9.4 mag star that limits the detection due to high background. The star is only $107''$ away from the position of the afterglow of GRB 060729. Figure 1 displays the 550 ks exposure UVW1 image of the field around GRB 060729.

In all bands, XRT as well as in all 6 UVOT filters, a significant break occurs in the light curve. Table 5 lists the decay slopes α_2 and α_3 before and after the break time T_{break} . Within the errors all break times seem to occur at about 50 ks after the burst (33 ks in the rest-frame), with the earliest break in B at about 30ks and the later breaks at shorter wavelengths. However, considering the uncertainties in the decay slopes, this is all consistent with an achromatic break. In B the afterglow decays the slowest with $\alpha_3=0.98$. The decay slopes at shorter wavelengths are steeper with $\alpha_3 \approx 1.3$. Note that the flatter slope in the B-Filter is caused by a re-brightening at about 200 ks that is not seen in the other filters. By limiting the analysis to data only up to 200ks the decay slope is $\alpha_3=1.17 \pm 0.16$ which is consistent with the decay slopes seen in the other filters. The re-brightening in B at about 200 ks after the burst seems to be real. We checked for any strong variability in the background but could not detect any strong background variation at that time.

Figure 9 displays the early UVOT and XRT light curves. The left panel of Figure 9 displays the UVOT White filter event mode and XRT WT mode data. The UVOT White filter data were grouped into 10 s bins. The first UVOT White points show a decay similar to the XRT WT light curve. However after these few points the UVOT White light curve flattens, which agrees with the flare seen in the XRT data at 170s after the burst. At about 200s after the burst the afterglow starts to become brighter in the UVOT White, while it is still decaying in X-rays.

The right panel of Figure 9 shows the UVOT V event mode data and the XRT PC mode data of the first orbit. The UVOT V data were grouped in 25 s bins and the XRT PC mode data with 25 source photons per bin. The UVOT V light curve shows the afterglow fairly constant at about 17.5 mag while the XRT PC mode light curves shows an initial decay until about 600s and flattens after that.

The *XMM-Newton* Optical Monitor observations are summarized in Table 6. While the U filter results agree well with the UVOT U data as listed in Table 4, there is a discrepancy in the UVW1 and UVM2 filters. There maybe two explanations for this discrepancy: 1) The OM and UVOT UV filter sets have different filter transmission, 2) OM suffers from significantly higher level of scattered light than the UVOT, and third the extraction radius of the automated OM software is $12''$ which is too large for an accurate analysis of the UV data due to the bright star (see UVOT section). The brightening of the afterglow in the last OM UVM2 observation at 101 ks after the burst is most likely due to a bad subtraction of the background within the automatic OM data reduction software.

3.5. Spectral Energy Distribution

As shown in section 3.4 the long-term light curves in all 6 UVOT filters and in X-rays do follow the same decay slope with similar break times at about 50 ks after the burst. In order to check this we determined spectral energy distributions (SEDs) of the afterglow at 800s, 20 ks, 100 ks, and 500 ks. Figure 10 displays these four SEDs. These times are also marked in Figure 8. These times were picked to represent the SEDs of the earliest and latest time possible when the afterglow was detected in all 6 UVOT filters and shortly before and after the break. All fluxes in all 6 UVOT filters and the XRT were calculated according to the light curves. There seem to be no obvious changes in the SEDs, besides the changes in the fluxes, over time. Another independent measure of any changes in the SEDs over time is the optical/UV to X-ray spectral slope or X-ray loudness³ β_{ox} . For the afterglow of GRB 060729 we measured rest-frame β_{ox} of 0.85 ± 0.10 at 800s, 0.84 ± 0.05 at 20 ks, 0.74 ± 0.07 at 100 ks, and 0.77 ± 0.10 at 500 ks after the burst. Within the errors these values are consistent and do not suggest any changes between the optical/UV and X-ray parts of the SED over time.

Assuming a single power law spectrum between optical/UV and X-ray energies a $\beta_{\text{ox}}=1.1$ is expected according to the fits to the X-ray data (Table 3). The difference between the expected to the

³The X-ray loudness is defined by Tananbaum et al. (1979) as $\beta_{\text{ox}} = -0.384 \log(f_{2\text{keV}}/f_{2500\text{\AA}})$.

measured β_{ox} values suggests intrinsic reddening at the location of the afterglow. Based on the absorption corrected rest-frame 2 keV flux density we can calculate the expected flux density at rest-frame 2500Å. We calculated a reddening of 1.7 mag at rest-frame 2500Å which corresponds to an $E_{\text{B-V}}=0.34$ mag. Applying the relation given by Diplás & Savage (1994)⁴ we calculated an intrinsic column density $N_{\text{H,intr}} = 1.7 \times 10^{21} \text{ cm}^{-2}$. Considering that this is a rough estimate, this absorption column Denis Ty agrees quite well with that measured from the *XMM-Newton* EPIC pn spectrum, $N_{\text{H,intr}} = 0.85 \pm 0.02 \times 10^{21} \text{ cm}^{-2}$ (Table 3).

4. Discussion

The afterglow of GRB 060729 has been detected in X-ray longer than any other *Swift*-detected burst. By the time of writing this manuscript (November 2006, 100 days after the burst) the afterglow is still detectable by the *Swift* XRT. The estimate is that it will still be detectable by the *Swift* XRT until the end of December 2006.

4.1. Light curves

The X-ray and UV/Optical light curves are remarkably similar. Not only that their decay slopes and break times are in good agreement (except for the B light curve), but they also seem to be synchronized during rebrightening phases, which can be seen best in the UVW2 light curve. In particular the re-brightening at about 15 ks after the burst clearly appears to be present in all 6 UVOT filters and in X-rays. Even though the break at around 50 ks after the burst seems to be achromatic, we do not consider this to be a jet break. The decay slope $\alpha_3=1.29$ is too shallow to be a jet break. It may also be that GRB 060729 is one of the bursts where a jet break will be absent as discussed by Willingale et al. (in preparation); Sato et al. (2007).

One of our main results is that the light curve of the afterglow does not yet show a jet break at 100 days after the burst (65 days in the rest frame). This is the longest period a GRB afterglow was ever followed and detected in X-rays, except for

⁴The Diplás & Savage (1994) relation is: $N_{\text{H}} = 4.93 \times 10^{21} \times E_{\text{B-V}} \text{ cm}^{-2}$.

GRB 030329 which was followed 258 days after the burst by *XMM-Newton* (Tiengo et al. 2004). According to the relation given in Willingale et al. (in preparation) we would have expected to see a jet break at about 5.5×10^6 s after the burst. With an isotropic energy in the rest-frame 1 keV-10 MeV $E_{\text{iso}} = 3.0 \times 10^{52}$ ergs and the relations given by Sari et al. (1999) and Frail et al. (2001), and the non-detection of a jet break, we derive that the opening angle of the jet has to be larger than 23° . With $\beta=1.0$ and $\alpha=1.34$ according to Table 2 in Zhang et al. (2006) we estimated an electron index slope $p=2.3$ for the ISM or wind case with $\nu > \max(\nu_m, \nu_c)$.

The afterglow of GRB 060729 is not only remarkable for its long follow-up observations in X-rays but also for its relatively late break time between the flat decay phase and the steepening phase (phases 2 and 3 according to Zhang et al. 2006; Nousek et al. 2006) at about 53 ks after the burst, which converts to 35 ks in the rest frame. Typically the break between phases 2 and 3 occurs around 10 ks after the burst (Nousek et al. 2006). The late time break at 35 ks after the burst (rest frame) requires a substantial ongoing injection of energy into the afterglow.

The relatively long time of this very flat decay ($\alpha_{X,2} = 0.14 \pm 0.02$) phase implies larger energy injection during the early time in this burst than in other bursts. This energy injection could be the result of refresh shock (Rees & Mészáros 1998) or continuous energy input from the central engine. Assume the energy injection has the form $L(t) \propto t^{-q}$, the light curve decay rate is $\frac{(2p-4)+(p+2)q}{4}$ for $\nu_X > \max(\nu_m, \nu_c)$ (Zhang et al. 2006). So we get $q \simeq 0$, and the total energy is increased by a factor of $(T_{\text{break},2}/T_{\text{break},1})^{1-q} \sim 100$ during this energy injection phase, where $T_{\text{break},1}$ and $T_{\text{break},2}$ are the first and second break time of the x-ray light curve respectively. Such a large energy increase factor is the highest among the *Swift*-detected GRBs (Nousek et al. 2006). This may be part of the reason that we see a bright x-ray afterglow for a very long time, besides that no jet break occurs before 100 days after the burst. The q value ($q = 0$) inferred for this burst implies a pulsar type (i.e. magnetic dipole radiation) energy injection (e.g. Dai & Lu 1998; Zhang & Mészáros 2001).

Using the X-ray luminosity $L_x = 2 \times 10^{46} \text{ erg s}^{-1}$ at $t = 10$ h, we estimate the isotropic ki-

netic energy at this time is $E_{k,iso} \sim 2.5 \times 10^{53}(\epsilon_e/0.1)^{-1}$ ergs (Freedman & Waxman 2001; Zhang et al. 2007), where ϵ_e is the equipartition factor of electrons in afterglow shocks. Assuming the energy increasing factor 100 during the flat decay phase, the isotropic kinetic energy before the energy injection phase is only $\sim 2.5 \times 10^{51}(\epsilon_e/0.1)^{-1}$ ergs, implying a high efficiency of gamma-ray production during the prompt phase. Using the isotropic kinetic energy and the jet break time larger than 100 days after the burst, we get the jet opening angle larger than $\theta_j \gtrsim 21^\circ n_{-1}^{1/8}$ (Frail et al. 2001), where $n_{-1} \equiv (n/0.1\text{cm}^{-3})$ is the number density of the circumburst ISM. From this, we further get the beam-corrected kinetic energy of the burst $E_{k,j} \gtrsim 1.7 \times 10^{52}$ ergs $(\epsilon_e/0.1)^{-1} n_{-1}^{1/4}$. Such a larger kinetic energy than those in usual bursts may be a direct consequence of the unusually long energy injection phase in the early time.

Even though the X-ray and UV/optical afterglow of GRB 060729 was unusually bright, it was rather unspectacular in the BAT 15-150 keV energy range. The fluence of 3×10^{-6} ergs cm^{-2} (Parsons et al. 2006) is rather moderate compared to other *Swift*-discovered bursts. Also note, that the peak luminosity of GRB 060729 of about 3×10^{50} ergs s^{-1} is very low for a long burst regarding the time lag between the 50-100 keV and 15-25 KeV band as shown by Gehrels et al. (2006).

The observations of the X-ray and UV fields of GRB 060729 have been the deepest ever performed by *Swift*. In X-rays we observed the field so far for 835 ks and in UVW1 for 550 ks, and 225 ks in UVW2. The UVW1 observation is the longest exposure were taken of any field in the UV by any UV observatory. The results of this study and the source identifications based on their spectral energy distributions will be presented in a separate paper which is preparation.

4.2. Spectra analysis of the early time data

During the XRT WT mode epoch of observations, two flares are detected. For the first X-ray flare, only the decay part is seen by the XRT. The decay rates after the peak of the flares are as steep as t^{-5} , pointing to internal central engine activity as the origin for the X-ray

flares (Burrows et al. 2005b; Fan & Wei 2005; Zhang et al. 2006; Dai et al. 2006; Falcone et al. 2006; Wu et al. 2006; Wang et al. 2006; Lazzati & Perna 2006).

During 130-160 s (time bins from 1 to 11 in Table 2) and 190-300 s, the X-ray emission is undergoing steep decay, which may result from the high-latitude emission of the corresponding flares (Kumar & Panaitescu 2000; Liang et al. 2006), i.e. we see the curvature effect of the radiation pulse. In this picture, the count rate and the peak energy (kT or E_{break}) both decrease as the pulse decays. This is because less and less Doppler-boosted radiation is seen from the pulse. This accounts for the correlation between the count rate and the peak energy.

The WT data of the early afterglow observations showed a dramatic change in the X-ray spectrum within less than two minutes in the rest frame. Typically the spectra of the bins of the WT mode data can be fitted by a single absorbed power law or a black body plus power law model. The power law model shows that there is a decrease in the absorption column density by a factor of 4 from the beginning of the observation at 131 s after the burst to 300s after the burst. Such decreases in the absorption column density have been observed before in GRB afterglows, like e.g. in GRB 050712 (De Pasquale et al. 2006), but have been usually linked to a flattening of the X-ray spectral slope. This is typically an artifact of the spectral fitting routine. However, the situation in GRB 060729 is completely different. Here we observe not only a decreasing absorption column density N_H , but also a steepening of the X-ray spectral slope β_X , which is the opposite of what one expects if this is just an artifact of the fitting routine. Therefore we consider the decrease of the absorption column density to be real. There are two explanations for a decrease in the column density of a neutral absorber: 1) an expanding medium which results in a lower volume and column density and 2) ionization of the neutral gas. Both, the expansion and the ionization of the gas, happen after the explosion of the star.

Alternatively the WT mode spectra can also be fitted with a black body plus power law model. In order to limit the number of free parameters the absorption column density parameter was set to the Galactic value. These fits show a decrease of

the black body temperature from about 0.6 keV to about 0.1 keV from the beginning to the end of the WT observing period. Fixing the absorption column density to a value of $1 \times 10^{21} \text{ cm}^{-2}$, the value obtained at later times during the XMM observation, results in similar values for the black-body temperature. From these fits the temperature tends to be slightly lower than when fixing the N_H to the Galactic value. However, within the errors the results are consistent. The biggest influence the increase in the absorption column density has is on the normalization of the blackbody and power law components.

In the latter scenario, the thermal component is likely to be the photospheric emission from X-ray flares. In the prompt GRB phase, we have seen the thermal emission from some bursts (e.g. Ryde et al. 2007), which has been interpreted as the photospheric emission when the fireball becomes optically-thin (Mészáros & Rees 2000; Rees & Mészáros 2005; Thompson et al. 2007). Since X-ray flares are believed to be the result of late-time central engine activity with radiation mechanism similar to the prompt phase, a photosphere component found in X-ray flares is reasonable. The thermal emission component discovered from GRB060729 also supports the internal origin of the X-ray flares, rather than external shocks. Let us examine the relation between the black body radius R_{bb} derived from the spectral fitting and the photosphere radius R_{ph} . For a relativistic moving source, the luminosity of the thermal component at the photospheric radius is

$$L = 4\pi R_{ph}^2 \Gamma^2 \sigma T'^4 \quad (1)$$

where T' is the photospheric temperature in the co-moving frame and Γ is the bulk Lorentz factor. As the usual fitting uses $L = 4\pi R_{bb}^2 \sigma T^4$, we get $R_{ph} = \Gamma R_{bb}$ by taking advantage of $T = \Gamma T'$. The fitted black body radii around the peak of the X-ray flares are a few times 10^{12} cm . This means the photospheric radii of the two X-ray flares in GRB060729 are a few times of $10^{12} \Gamma \text{ cm}$. The photospheric radius is very sensitive to the bulk Lorentz factor Γ of the fireball (Rees & Mészáros 2005) and a photospheric radius of $10^{13} - 10^{14} \text{ cm}$ is reasonable if Γ of the X-ray flare is of the order of ten.

During the steep decay phase, the bolometric flux (equivalent to the flux in XRT band if the

peak energy located within the 0.3-10 KeV range of the XRT) may decrease as $F_X(t) \propto (t - t_0)^{-2}$ due to the curvature effect (Ryde & Petrosian 2002), where t_0 is some reference time of the flare (Liang et al. 2006), and the peak energy decays as $(t - t_0)^{-1}$. So if we fit the spectrum with the black body model ($F_X(t) \propto T^4 R_{bb}^2$) all the time during the decay phase, we would expect that the black body radius increases with time as $R_{bb} \propto (t - t_0)$. This may explain the apparent increase of the black body radius with time during the steep phase of the flares.

5. Conclusions and Summary

We studied the *Swift* and *XMM-Newton* observations of the afterglow of GRB 060729 and found:

- The light curve of the afterglow extends out to 100 days after the burst (65 days in the rest-frame) without showing any sign of a jet break. We estimated that the jet opening angle has to be larger than 23° . This is the longest followup and detection of a GRB afterglow ever performed, except for GRB 030329.
- The X-ray light curve can be generally described by an initial steep decay slope $\alpha_1=5.1\pm0.2$, a break time $T_{\text{break},1}=530\pm25$ s, flat decay slope $\alpha_2=0.1$ with a break at $T_{\text{break},2}=56.8\pm10$ ks, and a steep decay slope $\alpha_3=1.3$.
- The unusually long flat decay phase of the afterglow of GRB 060729 implies a much larger energy injection than seen in any other GRB afterglow.
- After the initial phase, the light curves in X-rays as well as in all 6 UVOT filters follow the same shape.
- In the initial phase the afterglow shows a dramatic change in its X-ray spectrum which can either be described by a steepening of a power law spectrum with a simultaneous decrease in the intrinsic column density, or a decrease in the black body temperature from 0.6 keV at 130s after the burst to 0.1 keV at 250s observed after the burst.

- The spectral analysis of the *Swift* XRT PC mode and *XMM-Newton* EPIC pn and MOS data shows that the X-ray spectrum of the afterglow agrees with an absorbed power law with $\beta_X=1.1$ and an intrinsic column density $N_{H,intr} = 1 \times 10^{21} \text{ cm}^{-2}$.
- The reddening and intrinsic column density estimated from the spectral energy distribution agrees well with the value found from the *XMM-Newton* analysis.

We would like to thank Dmitry Frederiks for checking the Konus-Wind measurements of the time of the burst. This research has made use of data obtained through the High Energy Astrophysics Science Archive Research Center Online Service, provided by the NASA/Goddard Space Flight Center. This research was supported by NASA contract NAS5-00136 and SAO grant G05-6076X BASIC.

REFERENCES

- Abbey, T., 2006, proceedings of the conference “The X-ray Universe”, El Escorial, 2005, ESA-SP 604, p943
- Arnaud, K. A., 1996, ASP Conf. Ser. 101: Astronomical Data Analysis Software and Systems V, 101, 17
- Barthelmy, S.D., et al. 2005, Space Science Reviews, 120, 143
- Blustin, A.J., et al., 2005, ApJ, 637, 901
- Burrows, D.N., et al., 2005a, Space Science Reviews, 120, 165
- Burrows, D.N., et al., 2005b, Science, 309, 1833
- Burrows, D.N., et al. 2006a, ApJ, accepted, astro-ph/0604320
- Burrows, D.N., Moretti, A., Perri, M., Capalbi, M., Angelini, L., & Hill, J.E., 2006b, GCN 5750
- Campana, S., & De Luca, A., 2006, GCN 5469
- Campana, S., et a., 2006, Nature, 442, 1008
- Chester, M., et al., 2005, GCN 3670
- Cobb, B.E., & Bailyn, C.D., 2006, GCN 5465
- den Herder, J.W., et al., 2001, A&A, 365, L7
- Dai, Z.G., & Lu, T., 1998, A&A, 333, L87
- Dai, Z.G., Wang, X. Y., Wu, X. F. & Zhang, B., 2006, Science, 311, 1127
- De Pasquale, M., et al., 2006, MNRAS, 370, 1859
- Dickey, J.M., & Lockman, F.J., 1990, ARA&A, 28, 215
- Diplas, A., & Savage, B.D., 1994, ApJ, 427, 274
- Fan, Y. Z. & Wei, D. M., 2005, MNRAS, 364, L42
- Falcone, A. et al. 2006, ApJ, 641, 1010
- Frail, D.A., Kulkarni, S.R., Sari, R., et al., 2001, ApJ, 562, L55
- Freedman, D.L., & Waxman, E., 2001, ApJ, 547, 922
- Gehrels, N., et al., 2004, ApJ, 611, 1005
- Gehrels, N., et al., 2006, Nature in press, astro-ph/0610635
- Grupe, D., 2006, GCN 5369
- Grupe, D., et al., 2006, GCN 5365
- Haberl, F., Schwope, A.D., Hambaryan, V., Hasinger, G., & Motch, C., 2003, A&A, 403, L19
- Hill, J.E., et al., 2004, SPIE, 5165, 217
- Hogg, D., 1999, astro-ph/9905116
- Immler, S., 2006, GCN 5367
- Jansen, F., et al., 2001, A&A, 365, L1
- Kumar, P. & Panaitescu, A, 2000, ApJ, 541, L51
- Lazzati, D. & Perna, R. 2006, MNRAS, submitted, astro-ph/0610730
- Liang, E. et al. 2006, ApJ, 646, 351
- Mangano, V., et al., 2007, A&A, in preparation.
- Mason, K.O., et al., 2001, A&A, 365, L36
- Mészáros, P. & Rees, M. J. 2000, ApJ, 530, 292

- Nousek, J., Kouveliotou, C., Grupe, D., Page, K.L., et al., 2006, *ApJ*, 642, 389
- O'Brien, P.T., et al., 2006, *ApJ*, 647,1213
- Parsons, A., et al., 2006, *GCN* 5370
- Pagani, C., et al., 2006, *ApJ*, 645, 1315
- Quimby, R., Swan, H., Rujopakarn, W., and Smith, D.A., 2006, *GCN* 5366
- Quimby, R., Rykoff, E.S., 2006, *GCN* 5377
- Rees, M.J., & Mészáros, P., 1998, *ApJ*, 496, L1
- Rees, M. J. & Mészáros, P. 2005, 628, 847
- Romano, P. et al. 2006, *A&A*, 456, 917
- Roming, P.W.A., et al., 2005, *Space Science Reviews*, 120, 95
- Ryde, F., Björnsson, C.-I., Kaneko, Y., Mészáros, P., Preece, R., & Battelino, M., 2007, *ApJ*, accepted, astro-ph/0608363
- Ryde, F. & Petrosian, V. 2002, *ApJ*, 578, 290
- Sato, G., et al., 2007, *ApJ*, accepted, astro-ph/0611148
- Sari, R., Piran, T., & Halpern, J.P., 1999, *ApJ*, 519, L17
- Schartel, N., 2006, *GCN* 5368
- Strüder, L., et al., 2001, *A&A*, 365, L5
- Tananbaum, H., et al., 1979, *ApJ*, 234, L9
- Thoene, C.C., et al., 2006, *GCN* 5373
- Thompson, C., Mészáros, P., & Rees, M.J., 2007, *ApJ*, submitted, astro-ph/0608282
- Tiengo, A., Mereghetti, S., Ghisellini, G., Tavocchio, F., Ghirlanda, G., 2004, *A&A*, 432, 861
- Turner, M.J.L., Abbey, A., Arnaud, M., et al., 2001, *A&A*, 365, L27
- Vaughan, S., et al., 2006, *ApJ*, 638, 920
- Wang, X. Y., Li, Z. & Mészáros, P., 2006, *ApJ*, 641, L89
- Willingale, R., et al., 2007, *ApJ*, to be submitted
- Wu, X. F. et al. 2006, *ApJ*, astro-ph/0512555
- Zhang, B., & Mészáros, P., 2001, *ApJ*, 552, L35
- Zhang, B., & Mészáros, P., 2004, *Int. Journal of Modern Physics A*, Vol. 19, No. 15, 2385
- Zhang, B., Fan, Y.Z., Dyks, J., Kobayashi, S., Mészáros, P., Burrows, B.N., Nousek, J.A., & Gehrels, N., 2006, *ApJ*, 642, 354
- Zhang, B., et al., 2007, *ApJ*, in press, astro-ph/0610177

Fig. 1.— UVW1 image ($5'.7 \times 4'.2$) of the field of GRB 060729 with an exposure of 550 ks. The circles displays the XRT position as given in Section 3.1. The circle in the large image shows a $10''$ radius just for display purposes, and the zoom-in image ($80'' \times 60''$) in the upper right corner shows the $3''.5$ XRT error radius. Note the bright star which is only $107''$ away from the position of the afterglow of GRB 060729. **Due to the size restrictions on atrop-h we could not include this figure.**

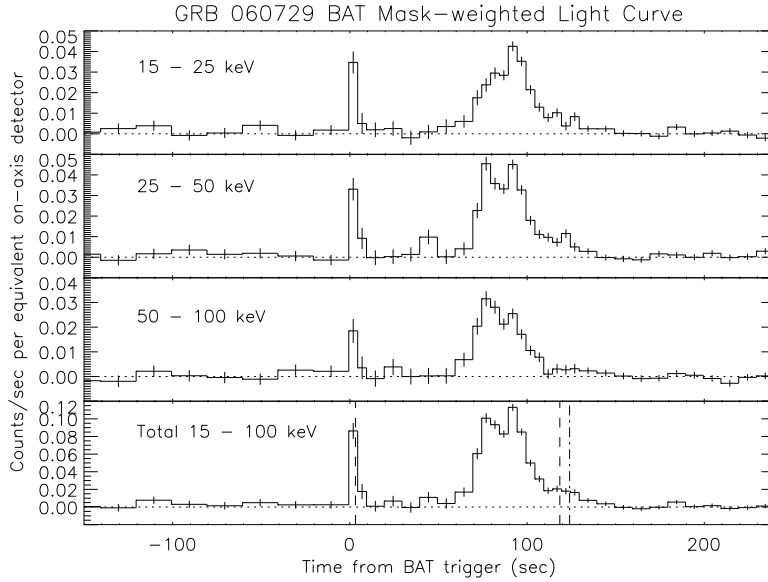


Fig. 2.— *Swift* BAT light curves in the 15–25 keV band (top), 25–50 keV (second panel), 50–100 keV (second lower panel), and in the 15–100 keV band (bottom). The vertical lines in the 15–100 keV plot mark the times for which T_{90} was calculated and the beginning of the XRT observations at 124s after the burst.

TABLE 1
SPECTRAL FITS TO THE BAT DATA. THE BAT DATA HAVE BEEN DIVIDED INTO 5 SEGMENTS AS LISTED BELOW.

| spectrum | T after trigger | $\beta_{15-150\text{keV}}$ | χ^2/ν | 15–150 keV | Flux ¹ | | Fluence ² | |
|-------------|-----------------|----------------------------|--------------|----------------------|-----------------------------|----------------------|-----------------------------|------------|
| | | | | | 1 keV – 10 MeV ³ | 15–150 keV | 1 keV – 10 MeV ³ | 15–150 keV |
| 1st flare | 0 – 10 | $1.05^{+0.42}_{-0.37}$ | 57/56 | 3.2×10^{-8} | 1.4×10^{-6} | 3.2×10^{-7} | 1.4×10^{-5} | |
| 2nd flare | 70 – 88 | $0.59^{+0.11}_{-0.11}$ | 59/56 | 5.8×10^{-8} | 4.5×10^{-7} | 1.0×10^{-6} | 8.1×10^{-6} | |
| 3rd flare | 88 – 124 | $0.90^{+0.11}_{-0.11}$ | 50/56 | 2.8×10^{-8} | 1.2×10^{-7} | 1.0×10^{-6} | 4.4×10^{-6} | |
| XRT flare 1 | 124 – 160 | $1.26^{+1.58}_{-0.86}$ | 49/56 | 2.6×10^{-9} | 1.2×10^{-8} | 9.4×10^{-8} | 4.2×10^{-7} | |
| XRT flare 2 | 180 – 190 | $1.59^{+5.23}_{-1.67}$ | 53/56 | 1.8×10^{-9} | 1.8×10^{-8} | 1.8×10^{-8} | 1.8×10^{-7} | |

¹15-150 keV flux in units of $\text{ergs s}^{-1} \text{cm}^{-2}$

²Fluence in units of ergs cm^{-2}

³Rest-frame 1 keV - 10 MeV (0.65 keV - 6.5 MeV observed)

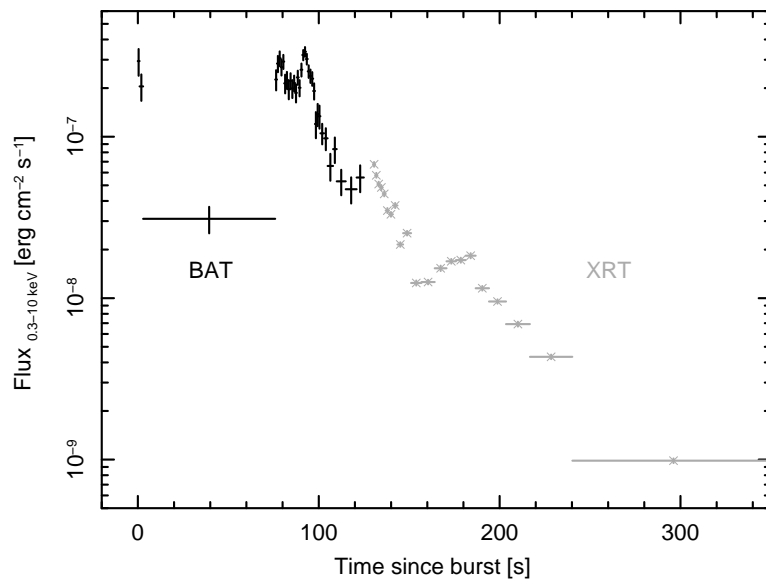


Fig. 3.— Combined *Swift* BAT and XRT WT light curves. The Figure clearly shows that the XRT was starting observing GRB 060729 during the fourth peak seen in the BAT.

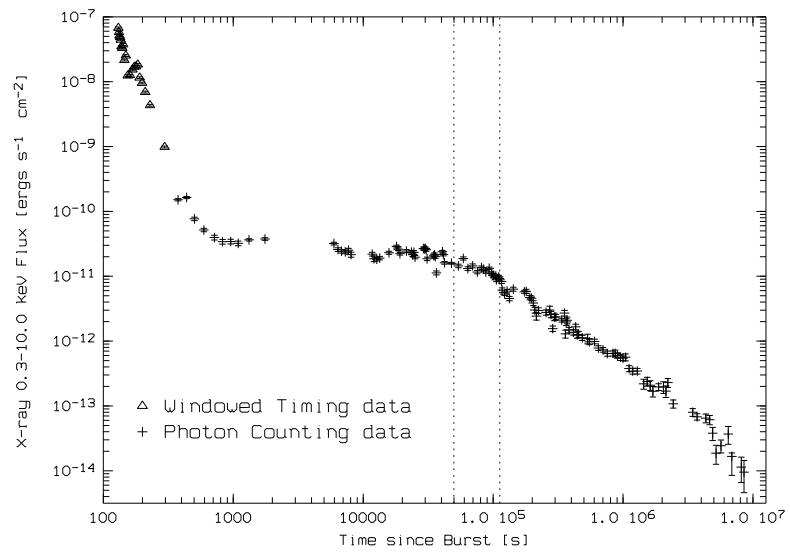


Fig. 4.— *Swift* XRT light curve of the Windowed Timing (triangles) and photon counting (crosses) mode data up to 2006 October 31. The dotted vertical lines mark the start and end times of the *XMM-Newton* observation.

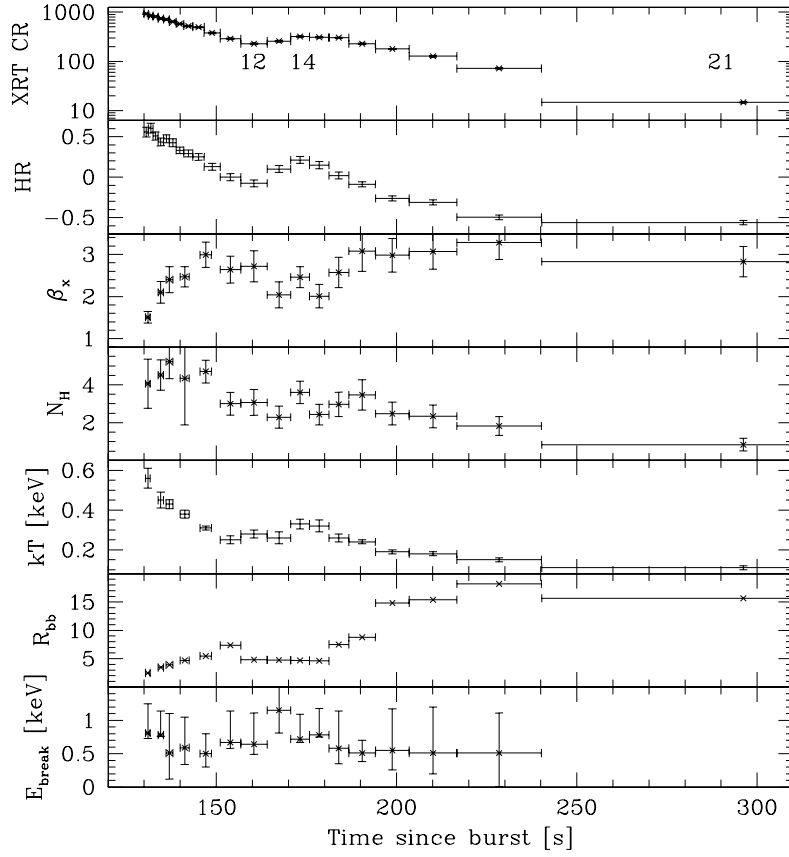


Fig. 5.— *Swift* XRT Windowed Timing mode light curve. The panels display from the top to the bottom the XRT count rate (in units of counts s^{-1}), the hardness ratio (see text for definition), the X-ray spectral slope β_X of a single power law fit, the free fit column density N_H in units of 10^{21} cm^{-2} , the blackbody temperature kT , the blackbody radius R_{bb} (in units of 10^{12} cm), and the cut off energy E_{break} of a power law with exponential cutoff. All these fit parameters are listed in Table 2. The numbers in the top panel mark the bins that were used for the spectra shown in Figure 6.

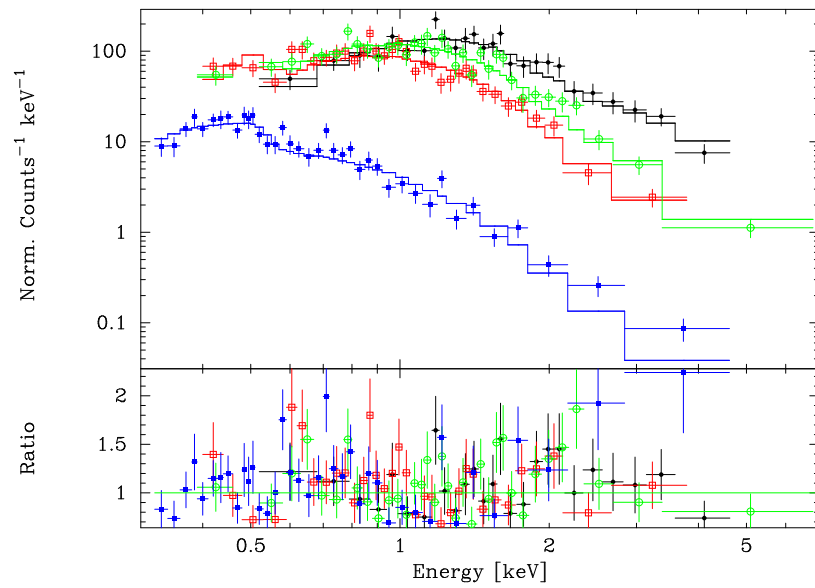


Fig. 6.— *Swift* XRT WT spectra of bins 1+2 (black filled circles), 12 (red open squares), 14 (green open circles), and 21 (blue filled squares) fitted by absorbed single power laws as given in Table 2. The numbers refer to the bins as shown in Figure 5.

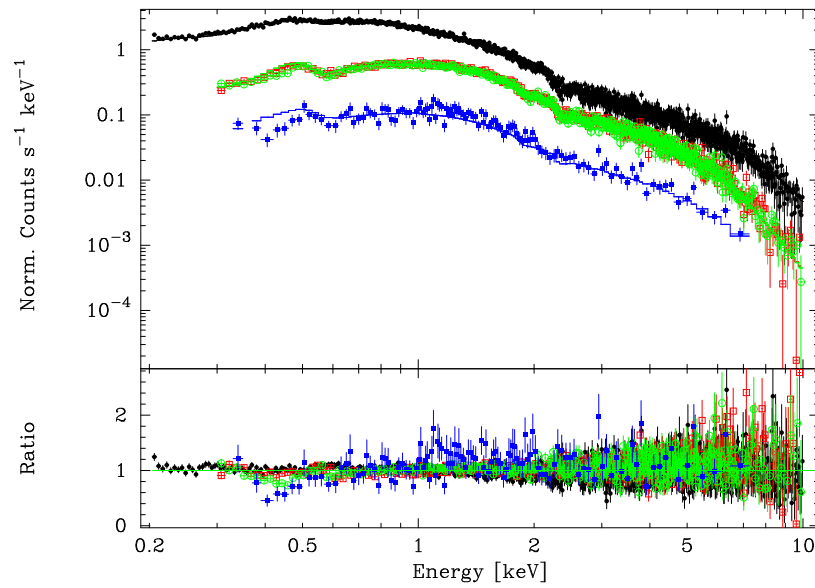


Fig. 7.— *XMM-Newton* EPIC pn (black filled circles), MOS1 (red open squares), MOS2 (green open circles), and *Swift* XRT PC mode (blue filled squares) spectra. The *Swift* XRT data were selected between 49.9 ks to 112.5 ks after the burst, simultaneous with the *XMM-Newton* observation.

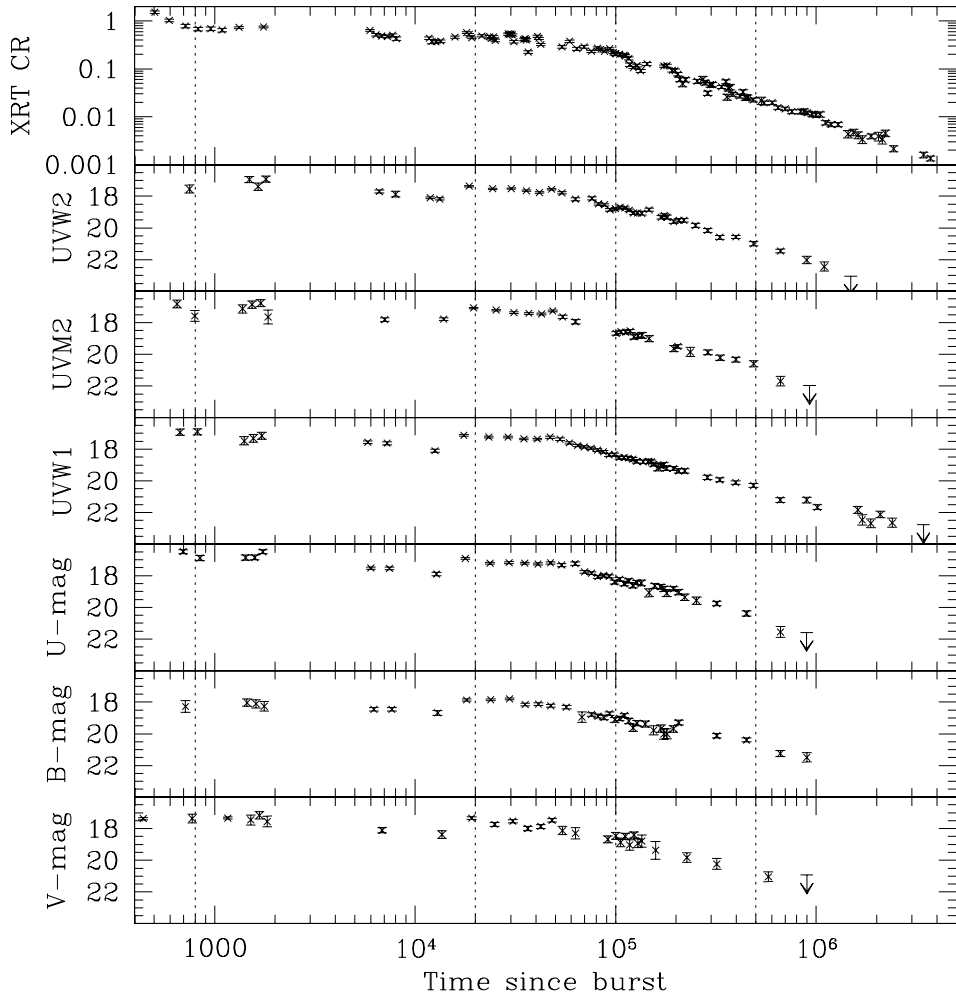


Fig. 8.— *Swift* UVOT and XRT PC mode light curves, with the XRT light curve on the top and the UVOT light curves starting with UVW2 on the top and V on the bottom. The downward arrows mark the 3σ upper limits as listed in Table 4. The vertical lines mark the times when the spectral energy distributions of the afterglow were determined as shown in Figure 10.

TABLE 2
SPECTRAL ANALYSIS OF THE 21 BINS OF THE *Swift* WT MODE DATA.¹

| Bin # | Time | T_{obs} | CR ² | HR ³ | Single Power Law | | | Blackbody + Power Law | | | Power Law with Exponential Cutoff | | |
|-------|------|------------------|-----------------|-----------------|--|--|--------------|--|----------------------|-------------------|-----------------------------------|--|--------------|
| | | | | | N_{H}^4 | β_{X} | χ^2/ν | kT ⁵ | bb-Flux ⁶ | R_{bb}^7 | χ^2/ν | E_{cutoff}^8 | χ^2/ν |
| 1 | 131 | 1.2 | 919±30 | 0.55±0.06 | 4.06 ^{+1.39} _{-1.15} | 1.51 ^{+0.35} _{-0.31} | 21/23 | 0.56 ^{+0.05} _{-0.04} | 7.46 | 2.49 | 16/23 | 0.82 ^{+0.44} _{-0.08} | 15/23 |
| 2 | 132 | 1.2 | 841±28 | 0.60±0.06 | | | | | | | | | |
| 3 | 133 | 1.4 | 807±27 | 0.51±0.05 | 4.51 ^{+0.88} _{-0.77} | 2.10 ^{+0.29} _{-0.25} | 39/32 | 0.45 ^{+0.04} _{-0.03} | 6.13 | 3.46 | 51/32 | 0.78 ^{+0.36} _{-0.02} | 48/32 |
| 4 | 135 | 1.6 | 737±25 | 0.43±0.05 | | | | | | | | | |
| 5 | 136 | 1.6 | 712±24 | 0.47±0.05 | 5.22 ^{+0.98} _{-0.85} | 2.40 ^{+0.33} _{-0.30} | 36/31 | 0.43 ^{+0.02} _{-0.02} | 6.23 | 3.91 | 34/31 | 0.51 ^{+0.59} _{-0.39} | 33/31 |
| 6 | 138 | 1.8 | 635±22 | 0.42±0.05 | | | | | | | | | |
| 7 | 140 | 2.1 | 579±19 | 0.33±0.04 | 4.35 ^{+0.58} _{-0.53} | 2.47 ^{+0.24} _{-0.21} | 39/46 | 0.38 ^{+0.02} _{-0.02} | 5.72 | 4.69 | 45/46 | 0.59 ^{+0.46} _{-0.25} | 45/46 |
| 8 | 142 | 2.6 | 520±18 | 0.29±0.04 | | | | | | | | | |
| 9 | 145 | 3.1 | 498±16 | 0.25±0.04 | 4.70 ^{+0.65} _{-0.58} | 2.99 ^{+0.32} _{-0.28} | 75/50 | 0.31 ^{+0.02} _{-0.02} | 3.60 | 5.48 | 96/50 | 0.50 ^{+0.3} _{-0.2} | 107/50 |
| 10 | 149 | 4.4 | 380±12 | 0.12±0.04 | | | | | | | | | |
| 11 | 154 | 5.7 | 289±10 | -0.00±0.04 | 3.00 ^{+0.62} _{-0.56} | 2.64 ^{+0.34} _{-0.30} | 29/34 | 0.25 ^{+0.02} _{-0.02} | 2.81 | 7.35 | 30/34 | 0.67 ^{+0.47} _{-0.09} | 33/34 |
| 12 | 161 | 7.3 | 227±7 | -0.07±0.04 | 3.07 ^{+0.71} _{-0.63} | 2.73 ^{+0.41} _{-0.36} | 43/32 | 0.29 ^{+0.02} _{-0.02} | 1.98 | 4.84 | 32/32 | 0.64 ^{+0.47} _{-0.15} | 34/32 |
| 13 | 167 | 6.4 | 258±9 | 0.10±0.04 | 2.29 ^{+0.60} _{-0.54} | 2.04 ^{+0.33} _{-0.29} | 38/32 | 0.27 ^{+0.03} _{-0.03} | 1.45 | 4.77 | 43/32 | 1.15 ^{+0.64} _{-0.34} | 48/32 |
| 14 | 173 | 5.2 | 320±10 | 0.21±0.04 | 3.60 ^{+0.62} _{-0.56} | 2.46 ^{+0.27} _{-0.24} | 40/33 | 0.34 ^{+0.03} _{-0.02} | 3.54 | 4.68 | 39/33 | 0.72 ^{+0.37} _{-0.05} | 37/33 |
| 15 | 179 | 5.4 | 310±10 | 0.15±0.04 | 2.43 ^{+0.59} _{-0.53} | 2.01 ^{+0.30} _{-0.28} | 39/35 | 0.32 ^{+0.03} _{-0.02} | 2.90 | 4.61 | 37/35 | 0.78 ^{+0.40} _{-0.03} | 35/35 |
| 16 | 184 | 5.5 | 301±10 | 0.02±0.04 | 2.97 ^{+0.67} _{-0.60} | 2.57 ^{+0.38} _{-0.34} | 35/34 | 0.26 ^{+0.02} _{-0.02} | 3.28 | 7.52 | 32/34 | 0.58 ^{+0.56} _{-0.23} | 36/34 |
| 17 | 190 | 7.4 | 227±7 | -0.09±0.03 | 3.46 ^{+0.85} _{-0.76} | 3.07 ^{+0.51} _{-0.46} | 55/35 | 0.24 ^{+0.01} _{-0.01} | 3.24 | 8.76 | 40/35 | 0.51 ^{+0.18} _{-0.13} | 45/35 |
| 18 | 199 | 9.4 | 178±5 | -0.26±0.03 | 2.48 ^{+0.62} _{-0.55} | 2.98 ^{+0.41} _{-0.36} | 62/39 | 0.19 ^{+0.01} _{-0.01} | 3.44 | 14.84 | 58/39 | 0.55 ^{+0.62} _{-0.29} | 60/39 |
| 19 | 210 | 14.0 | 127±4 | -0.31±0.03 | 2.34 ^{+0.63} _{-0.54} | 3.07 ^{+0.42} _{-0.36} | 59/38 | 0.18 ^{+0.01} _{-0.01} | 2.84 | 15.40 | 33/38 | 0.51 ^{+0.69} _{-0.31} | 60/38 |
| 20 | 229 | 23.4 | 72±2 | -0.50±0.03 | 1.83 ^{+0.53} _{-0.44} | 3.28 ^{+0.41} _{-0.35} | 72/36 | 0.15 ^{+0.01} _{-0.01} | 2.15 | 18.19 | 38/36 | 0.51 ^{+0.6} _{-0.5} | 76/36 |
| 21 | 296 | 112.0 | 14.8±0.4 | -0.56±0.03 | 0.84 ^{+0.35} _{-0.30} | 2.83 ^{+0.36} _{-0.32} | 64/37 | 0.11 ^{+0.01} _{-0.01} | 0.50 | 15.65 | 52/37 | — | — |

¹For the blackbody plus power law and the power law with exponential cutoff model the power law slope was fixed to $\beta_{\text{X}}=1.0$. For the blackbody plus power law model the absorption parameter was fixed to the Galactic value ($4.82 \times 10^{20} \text{ cm}^{-2}$ Dickey & Lockman 1990).

²Count rate CR in units of counts s^{-1} .

³The hardness ratio is defined as $HR = (\text{hard} - \text{soft})/(\text{hard} + \text{soft})$ where *soft* and *hard* are the photons in the 0.3-1.0 and 1.0-10.0 keV band, respectively.

⁴The column density N_{H} is given in units of 10^{21} cm^{-2} .

⁵Blackbody temperature in units of keV.

⁶The fluxes are given in units of $10^{-9} \text{ ergs s}^{-1} \text{ cm}^{-2}$.

⁷Blackbody radius R_{bb} given in units of 10^{12} cm .

⁸The break energy is given in units of keV.

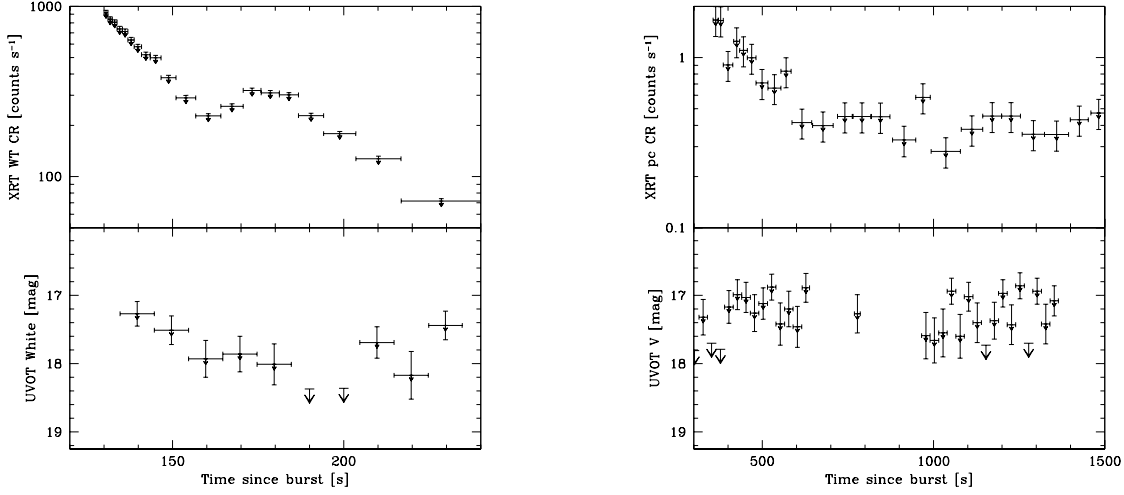


Fig. 9.— *Swift* UVOT White and V and XRT WT PC mode early time light curves of the first orbit. The left panel shows the UVOT White and the XRT WT mode data, and the right panel shows UVOT V and XRT PC mode data. The binning in the PC mode data is 25 photons per bin. The UVOT White data are binned in 10 s intervals and the V data are binned in 25 s intervals.

TABLE 3
SPECTRAL FITS TO THE *Swift* XRT AND XMM EPIC PN AND MOS DATA

| Detector | N_{H}^1 | β_{X} | χ^2/ν | $N_{\text{H, intr}}^2$ | β_{X} | χ^2/ν |
|---|-------------------------|------------------------|--------------|-------------------------|------------------------|--------------|
| <i>Swift</i> XRT ³ | $15.72^{+2.22}_{-2.10}$ | $1.19^{+0.09}_{-0.09}$ | 134/120 | $19.20^{+4.00}_{-3.72}$ | $1.11^{+0.08}_{-0.07}$ | 134/120 |
| XMM EPIC pn | $8.58^{+0.20}_{-0.20}$ | $1.12^{+0.01}_{-0.01}$ | 1159/1149 | $7.79^{+0.39}_{-0.38}$ | $1.11^{+0.01}_{-0.01}$ | 1124/1149 |
| XMM MOS1+MOS2 | $9.33^{+0.33}_{-0.32}$ | $1.04^{+0.02}_{-0.02}$ | 937/800 | $8.23^{+0.59}_{-0.58}$ | $1.01^{+0.01}_{-0.01}$ | 929/800 |
| XMM MOS 1+2 + <i>Swift</i> XRT | $9.54^{+0.32}_{-0.32}$ | $1.05^{+0.02}_{-0.02}$ | 1106/920 | $8.61^{+0.06}_{-0.06}$ | $1.02^{+0.01}_{-0.01}$ | 1097/920 |
| XMM pn + MOS1+2 + <i>Swift</i> XRT ³ | $8.57^{+0.17}_{-0.17}$ | $1.08^{+0.01}_{-0.01}$ | 2599/2071 | $7.55^{+0.03}_{-0.03}$ | $1.06^{+0.01}_{-0.01}$ | 2508/2071 |

¹The column density N_{H} at $z=0$ is given in units of 10^{20} cm^{-2} .

²Intrinsic column density $N_{\text{H, intr}}$ at the redshift of the burst, $z=0.54$, is given in units of 10^{20} cm^{-2} . The absorption column density at $z=0$ is set to the Galactic value, $4.82 \times 10^{20} \text{ cm}^{-2}$.

³The *Swift* XRT data were selected between 44.9-107.5 ks after the burst.

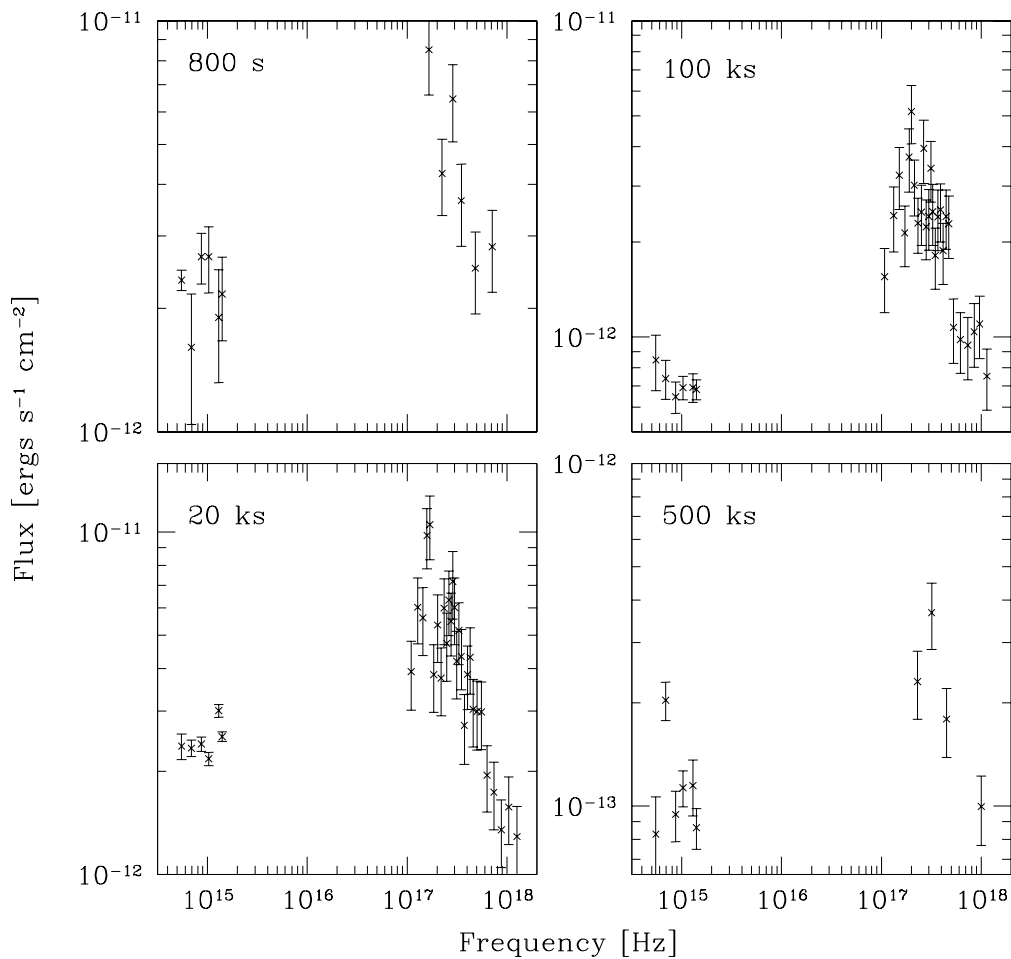


Fig. 10.— Spectral energy distributions of the afterglow of GRB 060729 at 800s (upper left), 20 ks (lower left), 100ks (upper right), and 500 ks (lower right). The UVOT photometry data are corrected for Galactic reddening.

TABLE 4

CENTRAL TIMES, EXPOSURE TIMES AND APERTURE CORRECTED MAGNITUDES OF THE UVOT LIGHT CURVES

| Bin # | V-Filter | | | B-Filter | | | U-Filter | | | UVW1-Filter | | | UVM2-Filter | | | UWV2-Filter | |
|-------|-------------------|-------------------------------|-------------------------|-------------------|-------------------------------|------------|-------------------|-------------------------------|-------------------------|-------------------|-------------------------------|------------------------|-------------------|-------------------------------|-------------------------|-------------------|-------------------------------|
| | Time ¹ | T _{exp} ² | Mag | Time ¹ | T _{exp} ² | Mag | Time ¹ | T _{exp} ² | Mag | Time ¹ | T _{exp} ² | Mag | Time ¹ | T _{exp} ² | Mag | Time ¹ | T _{exp} ² |
| 1 | 120 | 9 | 17.07±0.31 | 715 | 10 | 18.03±0.38 | 696 | 20 | 16.48±0.12 | 673 | 20 | 16.92±0.20 | 649 | 18 | 16.81±0.24 | 749 | 20 |
| 2 | 440 | 390 | 17.37±0.06 | 1451 | 20 | 18.10±0.23 | 844 | 20 | 16.88±0.15 | 820 | 20 | 16.89±0.20 | 796 | 20 | 17.57±0.33 | 1489 | 20 |
| 3 | 773 | 19 | 17.36±0.26 | 1609 | 20 | 18.26±0.36 | 1427 | 20 | 16.85±0.16 | 1403 | 20 | 17.47±0.26 | 1379 | 20 | 17.12±0.26 | 1647 | 20 |
| 4 | 1164 | 393 | 17.32±0.06 | 1767 | 20 | 18.45±0.30 | 1585 | 20 | 16.85±0.15 | 1561 | 20 | 17.31±0.24 | 1537 | 20 | 16.85±0.23 | 1695 | 19 |
| 5 | 1513 | 19 | 17.45±0.32 | 6224 | 197 | 18.45±0.10 | 1743 | 20 | 16.49±0.13 | 1719 | 20 | 17.14±0.23 | 1695 | 20 | 16.75±0.22 | 6834 | 197 |
| 6 | 1671 | 19 | 17.16±0.24 | 7657 | 197 | 18.68±0.11 | 6020 | 197 | 17.52±0.07 | 5815 | 197 | 17.55±0.09 | 1850 | 13 | 17.63±0.45 | 7998 | 63 |
| 7 | 1829 | 19 | 17.55±0.34 | 12919 | 134 | 17.86±0.14 | 7452 | 197 | 17.54±0.07 | 7247 | 197 | 17.62±0.09 | 7043 | 197 | 17.80±0.12 | 11878 | 751 |
| 8 | 6838 | 197 | 18.10±0.16 | 18042 | 211 | 17.84±0.06 | 12778 | 134 | 17.89±0.11 | 12568 | 268 | 18.09±0.10 | 1388 | 377 | 17.76±0.09 | 13266 | 537 |
| 9 | 13613 | 134 | 18.38±0.25 | 23824 | 211 | 17.78±0.06 | 17822 | 211 | 16.91±0.05 | 17495 | 422 | 17.11±0.05 | 19550 | 600 | 17.07±0.05 | 18585 | 844 |
| 10 | 19128 | 211 | 17.33±0.09 | 29606 | 211 | 18.14±0.06 | 23603 | 211 | 17.20±0.06 | 23276 | 422 | 17.23±0.05 | 25338 | 599 | 17.20±0.05 | 24367 | 845 |
| 11 | 24911 | 211 | 17.73±0.11 | 35388 | 211 | 18.12±0.07 | 29387 | 211 | 17.17±0.06 | 29059 | 422 | 17.22±0.05 | 31109 | 600 | 17.37±0.06 | 30149 | 844 |
| 12 | 30692 | 211 | 17.53±0.10 | 41205 | 208 | 18.22±0.08 | 35167 | 211 | 17.20±0.06 | 34840 | 422 | 17.35±0.05 | 36892 | 599 | 17.40±0.06 | 35931 | 845 |
| 13 | 36475 | 211 | 17.98±0.13 | 47494 | 147 | 18.31±0.09 | 40989 | 207 | 17.26±0.06 | 40666 | 415 | 17.35±0.05 | 42681 | 587 | 17.45±0.06 | 41738 | 829 |
| 14 | 42273 | 207 | 17.86±0.13 | 56873 | 129 | 18.94±0.11 | 47340 | 147 | 17.18±0.07 | 47109 | 296 | 17.24±0.06 | 48550 | 416 | 17.25±0.06 | 47877 | 592 |
| 15 | 48259 | 147 | 17.47±0.11 | 67943 | 42 | 18.77±0.34 | 53746 | 83 | 17.32±0.10 | 52836 | 183 | 17.36±0.08 | 54427 | 229 | 17.63±0.10 | 54050 | 330 |
| 16 | 54265 | 83 | 18.12±0.26 | 75864 | 211 | 18.88±0.16 | 62872 | 69 | 17.24±0.11 | 58802 | 385 | 17.60±0.06 | 63155 | 177 | 17.93±0.14 | 62989 | 277 |
| 17 | 63099 | 69 | 18.29±0.35 | 81646 | 211 | 18.96±0.13 | 69860 | 211 | 17.75±0.08 | 64698 | 436 | 17.76±0.07 | 100500 | 603 | 18.66±0.11 | 76105 | 249 |
| 18 | 91349 | 223 | 18.68±0.22 | 87426 | 211 | 18.72±0.14 | 75644 | 211 | 17.84±0.08 | 69533 | 422 | 17.85±0.07 | 106280 | 599 | 18.57±0.11 | 82086 | 640 |
| 19 | 100080 | 211 | 18.45±0.22 | 93208 | 211 | 19.11±0.11 | 81426 | 211 | 18.07±0.10 | 75315 | 423 | 17.93±0.07 | 112060 | 597 | 18.58±0.11 | 87970 | 846 |
| 20 | 105860 | 211 | 18.87±0.28 | 98988 | 211 | 19.02±0.15 | 87206 | 211 | 17.98±0.10 | 81097 | 423 | 18.05±0.08 | 117840 | 600 | 18.52±0.10 | 93752 | 846 |
| 21 | 111650 | 211 | 18.49±0.19 | 104770 | 211 | 18.84±0.13 | 92987 | 211 | 18.03±0.10 | 86877 | 423 | 18.17±0.08 | 123630 | 600 | 18.90±0.13 | 99532 | 847 |
| 22 | 117430 | 211 | 19.03±0.32 | 110560 | 211 | 19.18±0.13 | 98767 | 211 | 18.40±0.12 | 92658 | 423 | 18.35±0.09 | 129410 | 601 | 18.81±0.12 | 105320 | 846 |
| 23 | 123210 | 211 | 18.40±0.20 | 116340 | 211 | 19.62±0.16 | 104550 | 211 | 18.23±0.11 | 98438 | 423 | 18.33±0.09 | 135340 | 294 | 18.79±0.17 | 111100 | 846 |
| 24 | 128990 | 211 | 18.92±0.27 | 122120 | 211 | 19.32±0.23 | 110340 | 211 | 18.50±0.14 | 104230 | 423 | 18.53±0.10 | 146960 | 342 | 18.99±0.19 | 116880 | 846 |
| 25 | 135120 | 111 | 18.77±0.38 | 127900 | 211 | 19.37±0.17 | 116120 | 211 | 18.33±0.12 | 110010 | 423 | 18.52±0.10 | 195280 | 737 | 19.62±0.20 | 122660 | 845 |
| 26 | 158090 | 156 | 19.36±0.56 | 140600 | 225 | 19.77±0.18 | 121900 | 211 | 18.60±0.16 | 115790 | 423 | 18.56±0.10 | 204280 | 189 | 19.48±0.11 | 128450 | 845 |
| 27 | 226950 | 941 | 19.82±0.29 | 154780 | 180 | 19.66±0.30 | 127680 | 211 | 18.43±0.12 | 121570 | 422 | 18.63±0.11 | 235840 | 471 | 19.84±0.29 | 134830 | 445 |
| 28 | 319820 | 1374 | 20.22±0.34 | 168380 | 211 | 20.00±0.24 | 134430 | 110 | 18.46±0.17 | 127360 | 423 | 18.76±0.11 | 288290 | 1550 | 19.86±0.16 | 146750 | 522 |
| 29 | 576790 | 5531 | 21.04±0.40 | 174170 | 209 | 20.00±0.32 | 146620 | 178 | 19.08±0.25 | 137350 | 412 | 18.79±0.12 | 331760 | 2240 | 20.21±0.18 | 168860 | 729 |
| 30 | 897975 | 2368 | 3σ _{ul} =20.92 | 179940 | 211 | 19.68±0.32 | 156590 | 211 | 18.64±0.15 | 145550 | 291 | 18.76±0.14 | 397970 | 3140 | 20.33±0.16 | 174710 | 839 |
| 31 | ... | ... | ... | 194290 | 275 | 19.29±0.20 | 168160 | 211 | 18.70±0.15 | 150480 | 423 | 18.78±0.12 | 487880 | 2980 | 20.59±0.20 | 180340 | 556 |
| 32 | ... | ... | ... | 206460 | 273 | 20.11±0.15 | 173950 | 209 | 18.84±0.16 | 154560 | 456 | 18.94±0.12 | 663250 | 8830 | 21.68±0.30 | 194650 | 1100 |
| 33 | ... | ... | ... | 319120 | 1374 | 20.38±0.14 | 179720 | 211 | 19.09±0.21 | 162860 | 261 | 19.18±0.19 | 926689 | 3976 | 3σ _{ul} =21.96 | 206810 | 1092 |
| 34 | ... | ... | ... | 449360 | 2304 | 21.23±0.13 | 194150 | 275 | 18.82±0.13 | 167830 | 423 | 19.04±0.13 | ... | ... | ... | 218500 | 8795 |
| 35 | ... | ... | ... | 662500 | 3619 | 21.48±0.20 | 206310 | 273 | 19.03±0.16 | 173630 | 420 | 18.98±0.13 | ... | ... | ... | 250410 | 1111 |
| 36 | ... | ... | ... | 897470 | 2368 | 21.23±0.29 | 221160 | 280 | 19.35±0.22 | 179390 | 423 | 19.20±0.15 | ... | ... | ... | 287670 | 2200 |
| 37 | ... | ... | ... | ... | ... | ... | 253230 | 361 | 19.57±0.23 | 193930 | 549 | 19.21±0.12 | ... | ... | ... | 331140 | 3288 |
| 38 | ... | ... | ... | ... | ... | ... | 318970 | 1374 | 19.75±0.13 | 206100 | 545 | 19.37±0.14 | ... | ... | ... | 397340 | 4561 |
| 39 | ... | ... | ... | ... | ... | ... | 449220 | 2304 | 20.39±0.16 | 220980 | 559 | 19.37±0.15 | ... | ... | ... | 487280 | 4656 |
| 40 | ... | ... | ... | ... | ... | ... | 662390 | 3622 | 21.55±0.35 | 286960 | 1100 | 19.77±0.14 | ... | ... | ... | 662770 | 13555 |
| 41 | ... | ... | ... | ... | ... | ... | 897363 | 2368 | 3σ _{ul} =21.58 | 330430 | 1648 | 19.93±0.13 | ... | ... | ... | 897780 | 9498 |
| 42 | ... | ... | ... | ... | ... | ... | ... | ... | ... | 396620 | 2276 | 20.09±0.11 | ... | ... | ... | 1099600 | 13675 |
| 43 | ... | ... | ... | ... | ... | ... | ... | ... | ... | 486600 | 2323 | 20.29±0.13 | ... | ... | ... | 1487290 | 17912 |
| 44 | ... | ... | ... | ... | ... | ... | ... | ... | ... | 662230 | 7331 | 21.20±0.15 | ... | ... | ... | ... | ... |
| 45 | ... | ... | ... | ... | ... | ... | ... | ... | ... | 897220 | 4748 | 21.20±0.18 | ... | ... | ... | ... | ... |
| 46 | ... | ... | ... | ... | ... | ... | ... | ... | ... | 1012900 | 17014 | 21.65±0.15 | ... | ... | ... | ... | ... |
| 47 | ... | ... | ... | ... | ... | ... | ... | ... | ... | 1614900 | 12901 | 21.82±0.22 | ... | ... | ... | ... | ... |
| 48 | ... | ... | ... | ... | ... | ... | ... | ... | ... | 1697900 | 14706 | 22.46±0.32 | ... | ... | ... | ... | ... |
| 49 | ... | ... | ... | ... | ... | ... | ... | ... | ... | 1874500 | 24764 | 22.68±0.27 | ... | ... | ... | ... | ... |
| 50 | ... | ... | ... | ... | ... | ... | ... | ... | ... | 2091400 | 20552 | 22.11±0.20 | ... | ... | ... | ... | ... |
| 51 | ... | ... | ... | ... | ... | ... | ... | ... | ... | 2394800 | 39794 | 22.63±0.38 | ... | ... | ... | ... | ... |
| 52 | ... | ... | ... | ... | ... | ... | ... | ... | ... | 3431882 | 44673 | σ _{ul} =22.76 | ... | ... | ... | ... | ... |

¹The times mark the middle of the time bin in s after the burst.²The exposure times T_{exp} are given in s.

TABLE 5
DECAY SLOPES¹ AND BREAK TIMES OF THE UVOT LIGHT CURVES.

| Filter | α_2 ² | T_{break} ³ | α_3 |
|--------|-------------------------|----------------------------------|------------------------|
| V | 0.24±0.05 | 40 ⁺¹⁵ ₋₁₅ | 1.21±0.09 |
| B | 0.16±0.05 | 30 ⁺²⁰ ₋₁₀ | 0.96±0.05 ⁴ |
| U | 0.41±0.07 | 54 ⁺¹⁰ ₋₁₅ | 1.40±0.07 |
| UVW1 | 0.47±0.06 | 48 ⁺⁵ ₋₅ | 1.29±0.03 |
| UVM2 | 0.35±0.10 | 50 ⁺⁵ ₋₁₅ | 1.39±0.05 |
| UVW2 | 0.46±0.07 | 55 ⁺⁵ ₋₁₀ | 1.36±0.04 |
| X-rays | 0.14±0.02 | 57 ⁺¹⁰ ₋₁₀ | 1.29±0.03 |

¹The decay slopes α_2 and α_3 follow the conventions in Zhang et al. (2006) and Nousek et al. (2006).

²Decay slope before the energy injection and rebrightening at 20 ks after the burst

³Time after the break in ks in the observed frame

⁴Note that when limiting the analysis of the late time decay slope α_3 to 50-200 ks after the burst, the decay slope is 1.17±0.16.

TABLE 6
LIST OF THE *XMM-Newton* OPTICAL MONITOR OBSERVATIONS

| ObsID | T_{obs} ¹ | Filter | Mag |
|-------|-------------------------------|--------|------------|
| 006 | 48351 | U | 17.27±0.02 |
| 018 | 52707 | U | 17.43±0.02 |
| 010 | 70984 | UVW1 | 17.53±0.04 |
| 015 | 75291 | UVW1 | 17.57±0.04 |
| 016 | 84105 | UVW1 | 17.71±0.04 |
| 020 | 88612 | UVW1 | 17.83±0.05 |
| 012 | 92919 | UVM2 | 17.89±0.12 |
| 014 | 97226 | UVM2 | 17.98±0.13 |
| 017 | 101533 | UVM2 | 17.73±0.11 |

¹The times note the middle of the observation in s after the burst